

The properties of Gd₂O₃-assembled silica nanocomposite targeted nanoprobes and their application in MRI

Yuanzhi Shao^{a,1}, Xiumei Tian^{b,c,1}, Wenyong Hu^a, Yongyu Zhang^b, Huan Liu^a, Haoqiang He^b, Yingying Shen^{b,c}, Fukang Xie^c, Li Li^{b,*}

^a State Key Laboratory of Optoelectronic Materials and Technologies, School of Physics and Engineering, Sun Yat-Sen University, Guangzhou 510275, People's Republic of China

^b State Key Laboratory of Oncology in South China, Imaging Diagnosis and Interventional Center, Cancer Center, Sun Yat-Sen University, 651 Dongfeng Road East, Guangzhou 510060, People's Republic of China

^c Department of Histology and Embryology, Zhongshan School of Medicine, Sun Yat-Sen University, Guangzhou 510080, People's Republic of China

ARTICLE INFO

Article history:

Received 23 April 2012

Accepted 27 May 2012

Available online 15 June 2012

Keywords:

Silica

Atomistic and Molecular modeling

Synthesis

Targeted nanoprobes

Biocompatibility and pharmacodynamics

ABSTRACT

The feasibility of the gadolinium-doped mesoporous silica nanocomposite Gd₂O₃@MCM-41 as a safe, effective MRI nanoprobes has been validated in the current investigation systematically from atomistic and molecular modeling to its synthesis and characterization on *in vivo* MR imaging and biocompatibility. The first-principles calculation indicates that it is nearly impossible for toxic Gd ions to dissociate freely from silica. The biocompatibility studies confirm that the nanocomposite is lack of any potential toxicity; the biodistribution studies reveal a greater accumulation of the nanocomposite in liver, spleen, lung and tumor than in kidney, heart and brain; the excretion studies show that the nanocomposite can be cleared nearly 50% via the hepatobiliary transport mechanism after 1.5 months of injection. A larger water proton relaxivity r_1 and a better T_1 -weighted phantom MR imaging capability were detected in the nanocomposite than in the commercially available gadolinium diethylenetriaminepentaacetate. The results demonstrate that the nanocomposite is superior to the commercial counterpart in terms of contrast enhancement with a satisfactory biocompatibility, and it has a high potential to be developed into a safe and effective targeted probe for *in vivo* molecular imaging of cancer.

Crown Copyright © 2012 Published by Elsevier Ltd. All rights reserved.

1. Introduction

Magnetic resonance imaging (MRI) has been widely used in clinical diagnosis because of its noninvasive detection with a high spatial resolution, and recent development in molecular imaging has generated a demand for a targeted nanoprobes with desired safety and efficiency *in vivo* [1–3]. The performance of MRI nanoprobes depends on the contrast medium adopted. Mesoporous nanoparticles have been investigated for various biomedical and biotechnological applications in the past few years, such as targeted drug delivery [4–6], gene [7,8] and controlled drug release [9], and carrier vector of the contrast agents [10–12]. Mesoporous silica, which is chemically inert with good biocompatibility, possesses a unique structure of porous order on nanoscale and atomic disorder with modifiable surface and tunable pore array, and therefore emerges as a potential candidate for MRI contrast agent when gadolinium is incorporated. Unfortunately, clinical applications of Gd-doped silica nanoparticles have reached a bottleneck due to

limited research in toxicity and pharmacokinetics [13–15]. Both *in vitro* and *in vivo* pre-clinical studies on toxicity of nanoparticles (nanotoxicity) are vital to assess safety of nanoparticles. Nanotoxicity, especially immunotoxicity, has thus emerged as one of the most important components of nanotechnology. Although the standardized assessments on immunotoxicity of nanomaterials in biomedical products have not yet been established, it becomes important to elucidate the immune response to these nanoparticles in the pre-clinical research [16–19].

The nanoprobes with high biological efficacy and low toxicity is most expected [20,21]. In general, toxicity of nanoparticles is generally related to two factors: 1) free metal toxic ions dissociated from nanoparticles; 2) severe aggregation of nanoparticles due to their large specific surface, specific physicochemical characteristic [22], and segregation of residual material [23]. Aggregation of nanoparticles not only increases its half-life in the blood [6] and clearance time by intravenous injection but also blocks flow through capillaries and venules, leading to potential dangers of arterial embolism.

Although some studies have reported the use of Gd-doped mesoporous silica nanoparticles as an MRI contrast medium and its application in disclosing cell viability and the MR imaging of the

* Corresponding author. Tel./fax: +86 20 87343476.

E-mail address: li2@mail.sysu.edu.cn (L. Li).

¹ Yuanzhi Shao and Xiumei Tian contributed equally to this work.

aorta [24–29], there is still a lack of systematical pre-clinical studies on biocompatibility and pharmacodynamics *in vitro* and *in vivo*.

In our previous work, we reported the synthesis and characteristics of two sorts of Gd-doped mesoporous silica, SBA-15 [27] and MCM-41 [30], as well as the isothermal water-adsorptive capability of MCM-41 by molecular dynamics simulation [30]. Unfortunately, their biocompatibility and nanotoxicity in association with Gd-doping have not yet been investigated. Neither known is the state of Gd atoms situated inside the mesopores of MCM-41 silica, although the cluster state of Gd_2O_3 was presumably existed for the convenience of molecular mechanics calculation. Toxic free Gd ions are too localized to be dissociated from nanoparticles if a strong chemical bond, e.g. covalent bond, forms between Gd and oxygen atoms of silica. First principles calculations (density functional theory) based on quantum mechanics are necessarily employed to address Mulliken charge distribution and electron population in order to reveal the bond between Gd and oxygen atoms mentioned above.

In this study, we perform a systematic pre-clinical study of the nanocomposite as a novel MRI contrast medium on the frame of mesoporous silica MCM-41 with self-assembled Gd_2O_3 cluster. We first modeled its atomistic and molecular structure and computed its performance by molecular dynamic simulation and first-principle calculations. The nanocomposite was prepared by a one-step synthetic method and its structure and performance were characterized in comparison with its *in silico* counterpart. We also investigated the safety and efficiency of the nanocomposite systematically, which include its biocompatibility *in vitro* and *in vivo*, its pharmacokinetics and pharmacodynamics.

The paper is also supported by a supplementary information (SI) file that contains seven figures and two tables and is available online.

2. Methods and materials

2.1. Modeling and simulation, synthesis and characterization of $\text{Gd}_2\text{O}_3/\text{MCM-41}$ silica nanocomposite

The detailed theoretical modeling process as well as the typical procedures for the synthesis and characterization of $\text{Gd}_2\text{O}_3/\text{MCM-41}$ silica nanocomposite are given in the supplementary data (SD 1.1–1.3).

2.2. *In vitro* studies

Various Cell lines were grown in Dulbecco's modified Eagle's medium (DMEM), at 37 °C, 5% CO_2 . Cells in logarithmic growth period were used for assay.

2.2.1. Cytotoxicity

The mouse fibrosarcoma cell line L-929 and the murine macrophage line RAW264.7 were used for cell viability studies. Cells in 96-well plates were treated with different concentrations of $\text{Gd}_2\text{O}_3/\text{MCM-41}$ silica nanocomposites (10 μM , 1 μM and 100 nM), compared with untreated (culture media) and blank control (solvent). L-929 and RAW264.7 cells were then cultured for 48 h, whereas L-929 cells were also cultured for 72 h. At the end of incubation, 20 μL of MTT was added, and the cells were incubated for another 4 h. The culture medium was then carefully removed, and 100 μL dimethyl sulfoxide (DMSO) was added to each well to dissolve the formazan crystals for 10 min. The absorbance at 490 nm was measured by a microplate reader (Bio-Rad, USA).

2.2.2. Cell cycle assay

RAW264.7 cells were treated with different concentrations of $\text{Gd}_2\text{O}_3/\text{MCM-41}$ silica nanocomposites (5 μM , 100 nM), Gd-DTPA (5 μM , 100 nM) and dissolvant of carboxymethylcellulose sodium in culture media for 48 h. The cells were harvested and permeabilized by cold 70% ethanol (−20 °C) containing 10% FBS for 30 min. After two cold PBS washes, cells were labeled by propidium iodide (PI;

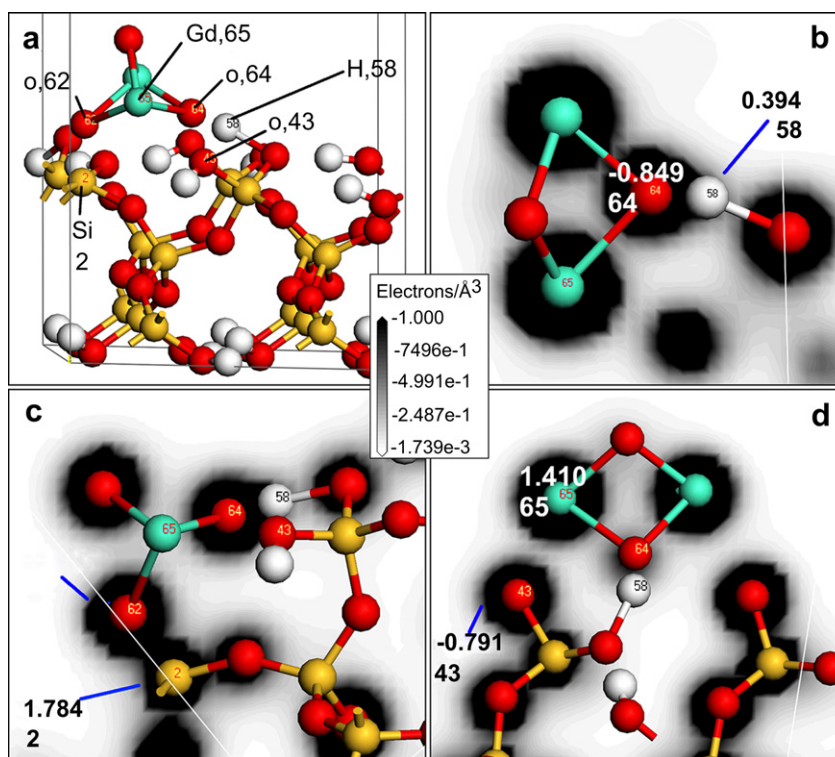


Fig. 1. Atomistic simulation and first-principle calculation of the combination of a Gd_2O_3 molecule and the silica SiO_2 . (a) Locations and orientations of atoms with numbering in the model; red, yellow, white and green atoms represent oxygen, silicon, hydrogen, and gadolinium atoms, respectively. A Gd_2O_3 molecule is adsorbed onto the silica matrix, and the adsorption energy is calculated as $E_a = -0.02966$ eV. (b–d) The electronic density of atoms. The top-down two atomic labels stand for Mulliken charge and atom numbering as specified in the model (a), respectively. (b) Existence of a high electronic density between the oxygen atom (No. 64) of Gd_2O_3 molecule and the hydrogen atom (No. 58) of silica matrix; (c) The highest electronic density between the oxygen atom (No. 62) of Gd_2O_3 molecule and silicon atom (No. 2) of silica matrix; (d) There is a certain electronic density between the gadolinium atom (No. 65, 66) with oxygen atom (No. 43, 41) of the silica matrix. A high electronic density between two atoms indicates a strong covalent bonding between two atoms.

Table 1

The Mulliken charge and population of electron shells of atoms before and after adsorption of Gd_2O_3 molecule. The atom label is presented in Fig. 1.

Atom label	Elements	Status	1s	2s	2p	3s	3p	3d	Mulliken charge
2	Si	After	—	—	—	0.494	1.209	0.504	1.794
		Before	—	—	—	0.520	1.396	0.516	1.568
62	O ^a	After	—	1.872	5.012	—	—	0.018	−0.905
		Before	—	1.924	4.871	—	—	0.018	−0.814
58	H	After	0.532	—	0.075	—	—	—	0.394
		Before	0.568	—	0.062	—	—	—	0.369
64	O ^a	After	—	1.810	5.024	—	—	0.016	−0.849
		Before	—	1.924	4.871	—	—	0.018	−0.814
43	O	After	—	1.786	4.985	—	—	0.020	−0.791
		Before	—	1.752	4.936	—	—	0.018	−0.704
Atom label	Elements	Status	5s	5p	4f	5d	6s	6p	Mulliken charge
65	Gd	After	2.000	6.000	7.344	0.970	0.095	0.179	1.410
		Before	2.018	6.016	7.332	1.275	0.066	0.073	1.221

^a Oxygen atom belonging to the Gd_2O_3 molecule.

Sigma–Aldrich) staining solution (50 $\mu\text{g}/\text{mL}$ PI and 0.1% Triton X-100 in PBS) in the dark for 10 min at room temperature before flow cytometry analysis. Lymphocytes were defined by FSC-H and SSC-H gating and further analyzed for cell cycle distribution. Cell cycle propagation, as determined by DNA ploidy, was assessed on the basis of PI incorporation. A minimum of 10,000 events was collected for each sample.

2.2.3. MRI of the nanocomposite

Hybrid nanoparticles were dispersed in 0.4% carboxymethylcellulose sodium with various $\text{Gd}_2\text{O}_3/\text{MCM-41}$ concentrations (1, 0.5, 0.25, 0.1, 0.05 and 0.025 mm/L). The array was embedded in a phantom consisting of a tank of water to allow appropriate image acquisition (Fig. 3c). After comparing with different concentrations of Gd-DTPA, we determined that the optimal concentration is 0.5 mm by the dose–response relationship. Moreover, signal density of the $\text{Gd}_2\text{O}_3/\text{MCM-41}$ is greatly stronger than that of Gd-DTPA, implying that the sensitivity of the contrast agents was enhanced effectively.

2.3. In vivo studies

2.3.1. Immunotoxicity assay of the nanocomposite

Assessing the compatibility with the immune system of nanobased biomedicine involves the evaluation of its physicochemical characteristics, some of them are listed in the following: as key mediators of immunity, reactive oxygen species (ROS) can regulate immune responses both positively or negatively [31], triggering either the eradication of pathogens or immunosuppression during wound-healing and tissue-restoration processes [32]. CD69 is an early T cell activation antigen [33]. As a protective role of B cells, CD80/CD86 is one of the co-stimulatory signals during the activation of T cells in primary immune responses [34].

Male BALB/c mice (6–8 weeks old) were purchased from the animal experiment center of the Medical College, Sun Yat-Sen University, China, and maintained in a specific pathogen-free (SPF) environment during the time of the experiments. Twenty-five mice were divided into 5 groups randomly: (1) Dissolvent, (2) Negative control (PBS 100 μL), (3) MCM-41 (16 $\mu\text{mol}/\text{kg}$), (4) $\text{Gd}_2\text{O}_3/\text{MCM-41}$ (16 $\mu\text{mol}/\text{kg}$), (5) positive control (lipopolysaccharide, LPS, Invitrogen), anti-mouse CD69-FITC, anti-mouse CD80/CD86-PE (Becton Dickinson PharMingen).

2.3.1.1. ROS of neutrophils assay. Peripheral blood (20 μL) was collected into a tube supplemented with heparin sodium (4 μL) by tail vein. Erythrocytes were then lysed (2 mL) in the samples in dark for 2 min, followed by the addition of 2 mL PBS. Samples were subsequently centrifuged at 1200 g for 5 min at room temperature, prior to the addition of H_2DCFDA (Invitrogen) to a final concentration of 5×10^6 mol/L. Cells were mixed thoroughly in dark for 20 min, prior to the addition of 400 μL PBS.

2.3.1.2. Expression of cytokine assay

2.3.1.2.1. Expression of CD80/CD86. Expression of CD80/CD86 was measured by flow cytometry. Peripheral blood (20 μL) was collected into a tube supplemented with heparin sodium (4 μL) by tail vein. Anti-mouse CD86-PE and anti-mouse CD80-PE were then added to the samples and incubated in dark for 30 min. Erythrocytes were lysed (2 mL) in dark for 2 min, followed by the addition of 2 mL PBS. Samples were subsequently centrifuged at 1200 g for 5 min at room temperature, followed by the addition of 400 μL PBS.

2.3.1.2.2. Expression of CD69. Expression of CD69 was measured by flow cytometry. Mice were sacrificed and lymphocyte cells were isolated from grounding submandibular, subclavicular, axillary, superficial inguinal and mesenteric lymph

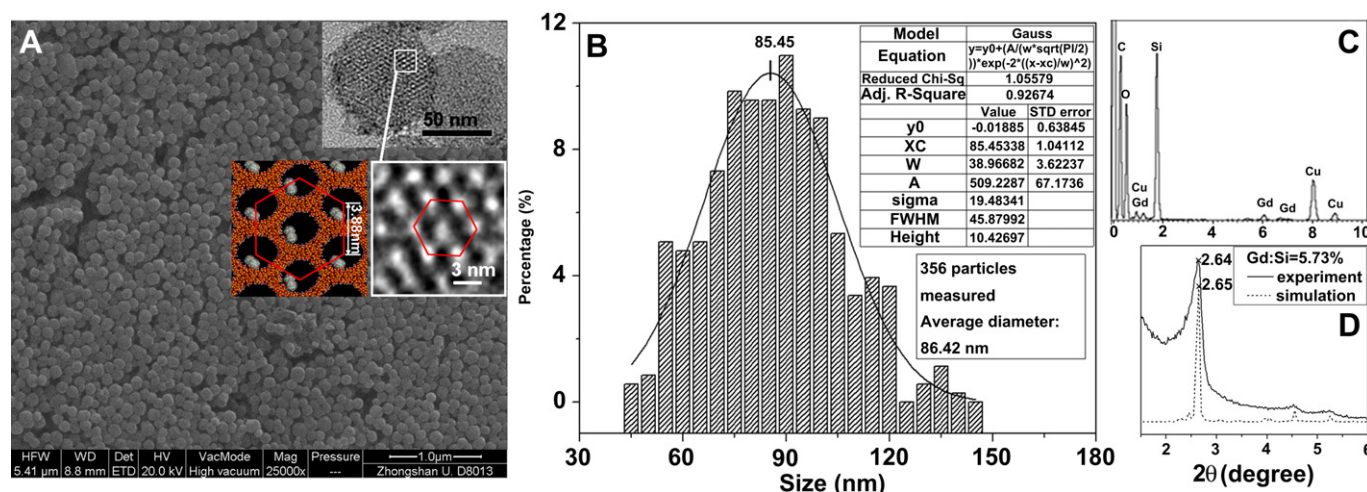


Fig. 2. Observed and simulated microstructures and the composition of $\text{Gd}_2\text{O}_3/\text{MCM-41}$ silica nanoparticles. (A) The overall morphology of the synthesized nanocomposites with a 5.7 at.% Gd doping; three insets included are two magnified HRTEM views of a $\text{Gd}_2\text{O}_3/\text{MCM-41}$ nanoparticle and its simulated supercell structure in which a Gd_2O_3 cluster consisted of five Gd_2O_3 molecules is adsorbed onto the inner surface of mesopores. The hexagonally-arrayed mesopores are outlined in red. (B) The size distribution calculated from the nanoparticles in (A). (C) The energy dispersive spectrum (EDS) measured within the synthesized nanoparticles indicates that Gd atoms are incorporated into the framework of MCM-41 silica. (D) The measured and simulated small-angle X-ray diffraction patterns of the synthesized nanoparticles and the supercell in Fig. 2(A); the intensity peak at $2\theta = 2.64$ – 2.65 corresponds to the spacing of hexagonally-arrayed mesopores, ~ 3.88 nm.

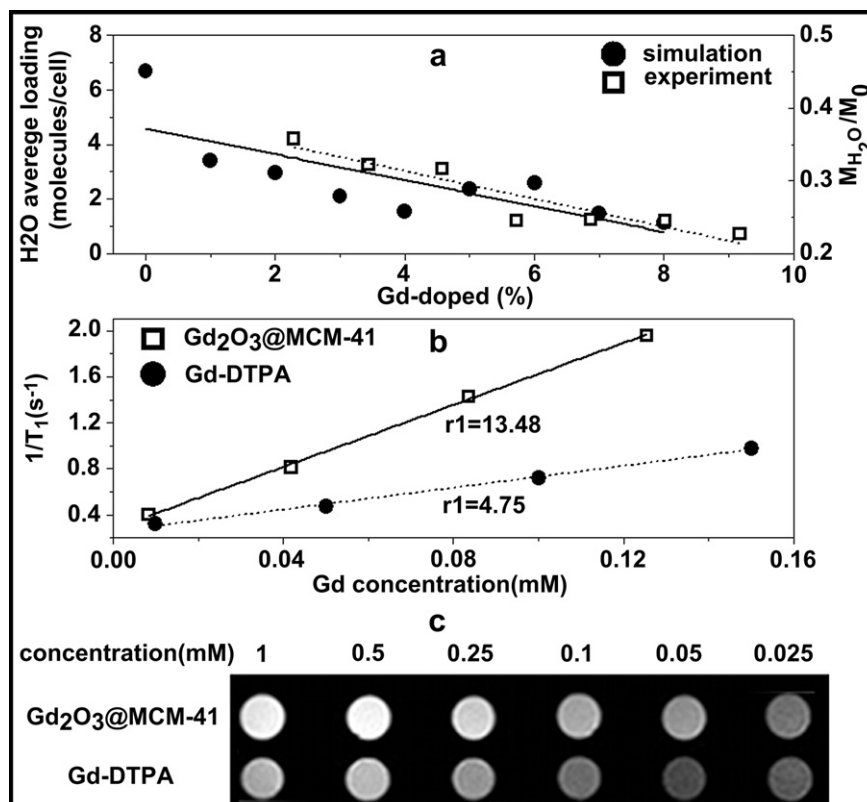


Fig. 3. (a) The average loading of water molecules of simulated models (left vertical axis) versus the water adsorption of experimentally measured samples (right vertical axis) in MCM-41 silica assembled with different additions of the Gd₂O₃ molecule. Comparison of the proton relaxivity r_1 (b) and T_1 -weighted phantom MR image (c) between Gd₂O₃@MCM-41 silica nanocomposite and the commercially available contrast agent Gd-DTPA.

nodes through 200 mesh under sterile conditions. Cells were then centrifuged at 300 g for 5 min at room temperature and incubated with anti-mouse CD69-FITC in dark for 30 min.

2.3.1.2.3. Expression of CD68 was measured by immunohistochemistry (IHC). Expression of the macrophage marker CD68 was analyzed by IHC in the liver of mice 48 h after injection of the nanocomposites (32 μ mol/kg) in 0.9% sodium chloride. Samples were formalin-fixed and paraffin-embedded, dewaxed, rehydrated, and blocked in 10% normal serum with 1% BSA in Tris-HCl buffer (TBS). According to the modified avidin-biotin-peroxidase complex (ABC) method [35], slides were incubated in anti-mouse CD68 (Abcam) 1:20 at 4 °C overnight, rinsed twice in TBS plus 0.025% Triton, and incubated with biotin-goat anti-Rat IgG (Invitrogen) 1:8000 with PBS (pH 7.4) containing 0.05% Tween 20 for 1 h at room temperature. After three 5 min washes in TBS, samples were developed with chromogen for 10 min at room temperature.

2.3.2. Acute toxicity test of the nanocomposite

Acute toxicity tests that determined the median lethal dose (LD₅₀) and 95% confidence limits were carried out on 70 clean Kunming white mice (female and male in half). Animals were provided by Animal Experiment Center of Sun Yat-Sen University and bred normally. Mice were randomly divided into 7 groups, and each group was injected by tail vein with different doses of Gd₂O₃@MCM-41 suspended in 0.4 percent sodium carboxymethylcellulose by ultrasonic oscillation (600 W, 5 min). Injected dose of six experiment groups is 99.43, 89.49, 80.54, 72.49, 65.24 and 58.71 mg/kg, respectively. The control group was administered 0.9 percent sodium chloride solution at 0.1 mL/10 g at the injection speed of 0.5 mL/min. Animals were investigated continuously for 14 days. Results were calculated by BSAS software based on the Bliss method.

2.3.3. Pharmacokinetic characteristics of the nanocomposite

2.3.3.1. Half-life of nanocomposite in the blood circulation. The half-life of the nanocomposite in the blood circulation was determined by ICP-MS ($n = 3$ for each point) in 33 clean Kunming white mice (50% females and 50% males). Sample preparation was similar to that of the acute toxicity test. Blood was drawn from the tail veins at 15, 30, 45, 60, 75, 120, 180, 240, 360, 480 and 600 min after tail vein administration of the nanocomposite (32 μ mol/kg). Blood (5–10 μ L) was collected at each time point and mixed immediately with heparin sodium (85 μ L) in eppendorf tubes. Samples were weighed prior to the addition of 5 mL nitric acid (HNO₃, Merk)

heated by an electric stove. After complete digestion and cooling, 2% HNO₃ was added to 25 mL for ICP-MS analysis. The calibration curve (SI Fig. 4) was plotted at the same time.

2.3.3.2. Biodistribution of the nanocomposite at the organ and subcellular level. At the organ level, concentration of gadolinium was measured by ICP-MS at 1, 4 and 10 h after nanocomposite injection (32 μ mol/kg) in the lung, heart, liver, spleen, kidney, brain and the nasopharyngeal carcinoma (NPC) xenografted tumor tissues ($n = 3$); at the subcellular level, TEM images were acquired 24 h after intravenous administration of Gd₂O₃@MCM-41 (32 μ mol/kg) in liver, spleen, lung, tumor, brain and kidney.

2.3.3.3. Excretion of the nanocomposite. Excretion of the nanocomposite was measured by ICP-MS, concentration of gadolinium was assayed after nanocomposite injection (32 μ mol/kg) in feces and urine of mice every week ($n = 3$) for 8 weeks.

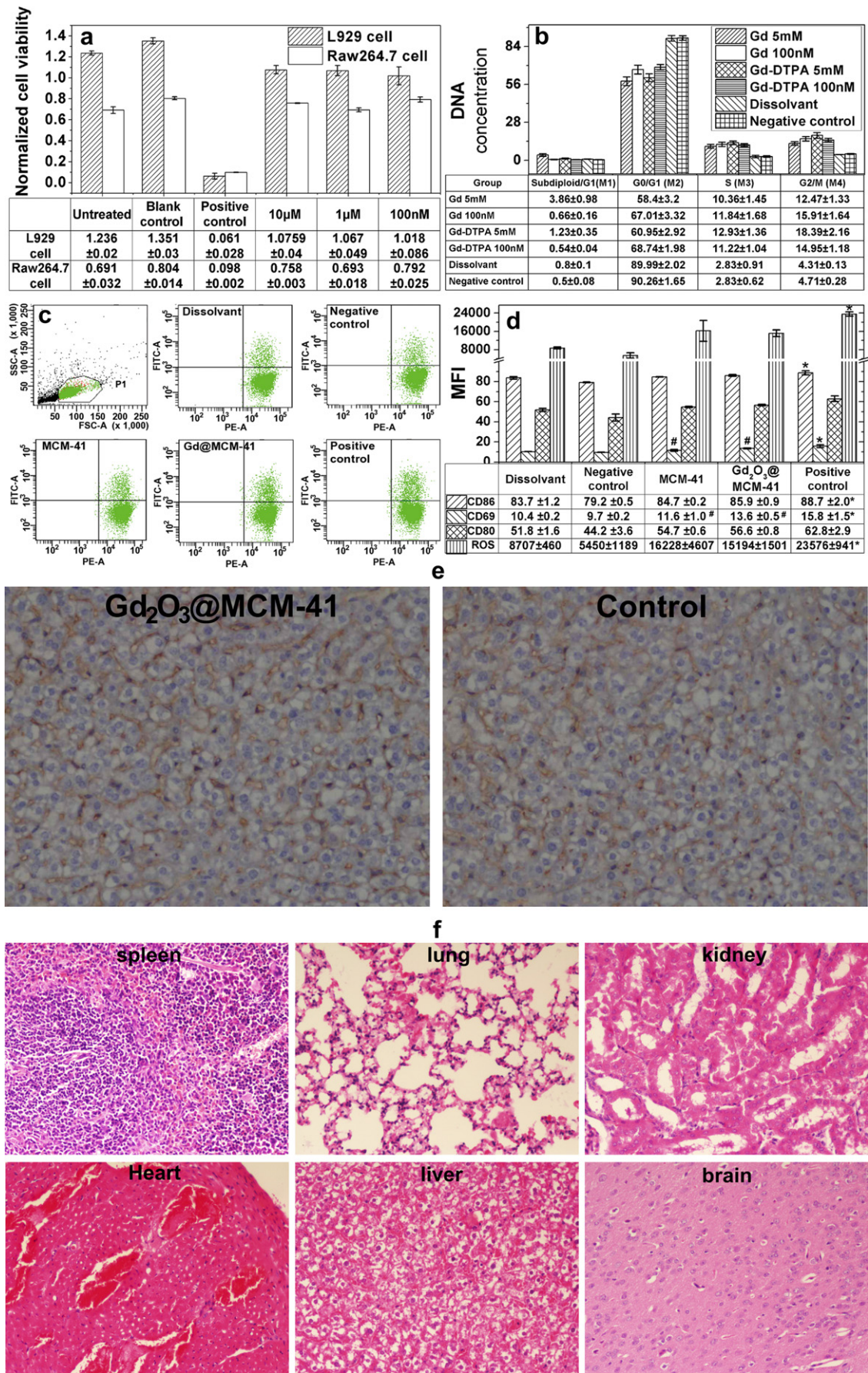
2.3.4. Animal model of MRI

Animal experiments were performed in accordance with the National Institutes of Health guidelines on the use of animals in research. Four to six-week-old Balb/c nude mice (with body weight of 19–23 g) were purchased from the animal experiment center of the Medical College, Sun Yat-Sen University, China, and maintained in a specific pathogen-free (SPF) environment (Certificate No. 26-99S029). Mice were injected subcutaneously with 5×10^6 nasopharyngeal carcinoma (NPC) CNE-2 cells in 100 μ L phosphate buffered saline (PBS/mouse). Nine days after tumor cell inoculation, mice were randomized by tumor size (approximately 70 mm³).

2.3.5. MR imaging

NPC mice were injected through the tail vein with 16 μ mol/kg of Gd₂O₃@MCM-41 in 100 μ L of 0.4% carboxymethylcellulose sodium and transported to a 3.0 T clinical scanner (Trio, Siemens) using a surface coil constructed specifically for small animals (3 inch in diameter). The control group was injected with 100 μ L saline solution.

T_1 -weighted images of the mouse bloodstream were obtained at 5, 15 and 30 min, and 1, 4 and 24 h after intravenous administration of Gd₂O₃@MCM-41. In all animals, T_1 -TSE with conventional k -space reading imaging was obtained in coronal and axial orientations. Sequences used were TSE T_1 coronal (5% dist. Factor, FOV 64 mm, slice thickness 2.0 mm, TR 700 ms, TE 12 ms, two averages) and TSE T_1 axial (5% dist. Factor, FOV 64 mm, slice thickness 2.0 mm, TR 600 ms, TE 12 ms, six averages).



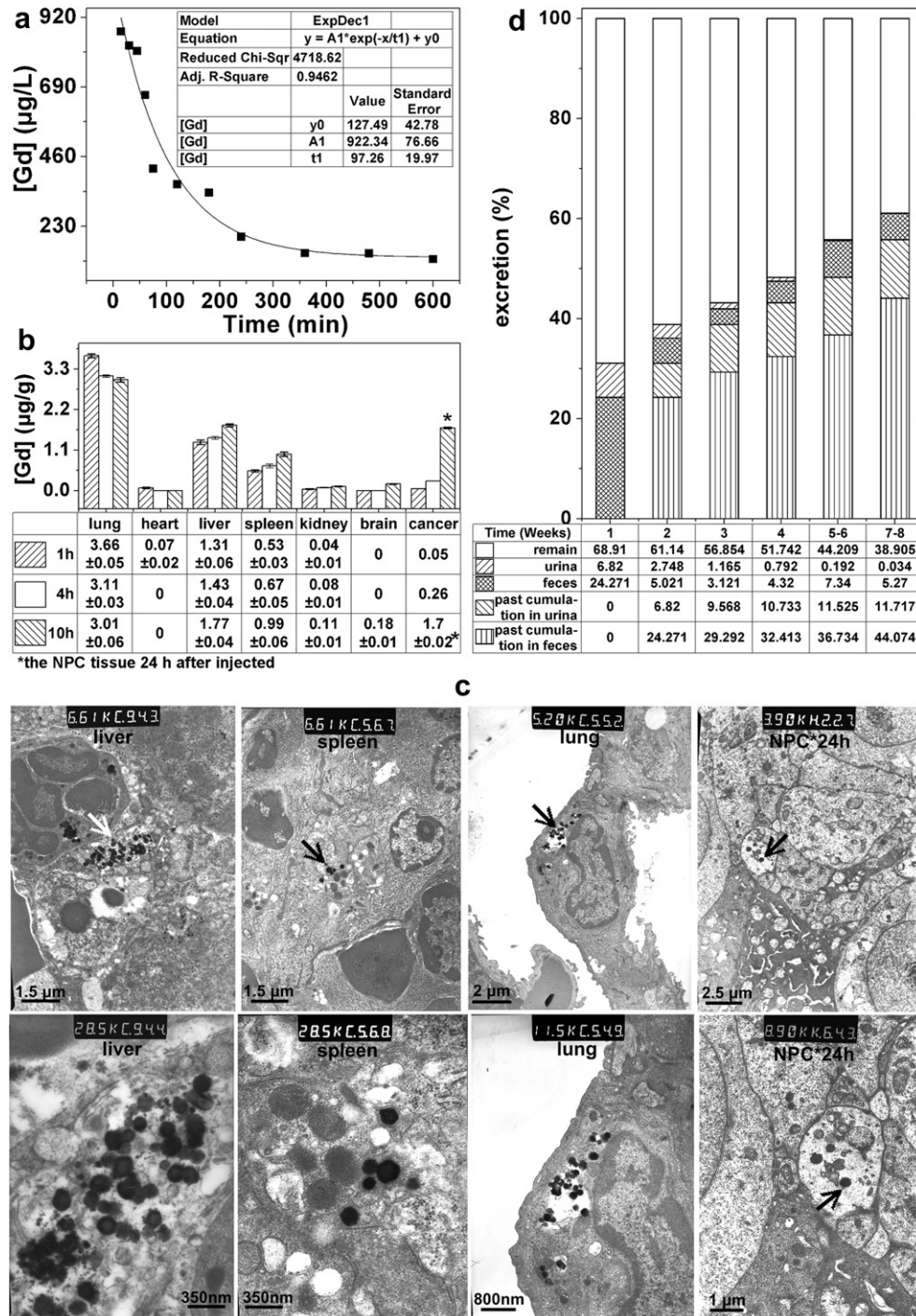


Fig. 5. Pharmacokinetics (half-life in blood, biodistribution and excretion) of $Gd_2O_3@MCM-41$ silica nanocomposite. (a) Determination of the half-life of $Gd_2O_3@MCM-41$ in blood. Concentration of gadolinium in the blood samples ($n = 3$) was measured by the ICP-MS; (b) Concentration of gadolinium was quantified in lung, heart, liver, spleen, kidney, brain and the NPC tissue ($n = 3$) 1, 4 and 10 h post-intravenous injection with the nanoparticles (32 $\mu\text{mol/kg}$); (c) TEM images of organs, 24 h after intravenous administration of $Gd_2O_3@MCM-41$ (32 $\mu\text{mol/kg}$). Nanoparticles are indicated by arrows; (d) Excretion of gadolinium was assayed in feces and urine of mice every week ($n = 3$).

Fig. 4. Nanotoxicity assays *in vitro*, including cell viability, cell cycle, apoptosis, and *in vivo* assays determining immunotoxicity and acute toxicity. (a) Cell viability of L-929 and RAW264.7 cells after incubation with different concentrations of $Gd_2O_3@MCM-41$ silica nanoparticles (10 μM , 1 μM and 100 nM) at 48 h (mean \pm SD, $n = 3$), compared with the untreated (culture media) and blank (solvent) controls; (b) Cell cycle analysis of RAW264.7 cells incubated with $Gd_2O_3@MCM-41$ (5 μM , 100 nM), Gd-DTPA (5 μM , 100 nM), dissolvant of carboxymethylcellulose sodium and culture media was determined at 48 h with mean fluorescence intensity (MFI) by flow cytometry at FL2-A channel (mean \pm SD, $n = 3$). Dead or apoptotic cells are found in the sub-diploid peaks (Sub-G1). Cells in G1 phase are found in diploid peaks; cells in S phase are found in the plateau area; and cells in G2/M are found in the polyploidy peaks; (c) Histogram plot of CD69 expression on T cells; (d) Analytical data on expression of CD69 in T cells and of CD80/CD86 in monocyte; ROS of neutrophils measured by flow cytometry at 48 h after injection in BALB/c mice (26.5 mg/kg, mean \pm SD, $n = 5$); (e) CD68 of macrophage surface factor were analyzed by IHC in mouse liver after injecting $Gd_2O_3@MCM-41$ (32 mg/kg) (left) and the 0.9% sodium chloride (right) under a light microscope at 200 \times magnification; (f) Acute toxicity test analysis was done using the tissues collected immediately after injecting the $Gd_2O_3@MCM-41$ (99.43 mg/kg), and determined by HE staining and observation under a light microscope at 200 \times magnification. Statistically significant differences between negative control group and others groups are as indicated (* $P < 0.05$; # $P < 0.01$).

All image data were transferred to a remote computer (PACS) for analysis. The entire tumor was selected from the dataset and used to generate normalized histograms of signal intensity. Using data from 2D MR studies ensured that the entire tissue of interest was examined and the results were not biased toward anomalously enhanced regions. The percentage enhancement was calculated for each of the images acquired.

2.4. Statistical analysis

The data were expressed as mean \pm SE and analyzed by *t*-test using excel 2007 software. The *p* value smaller than 0.05 was considered statistically significant. Except cell cycle analysis was performed using CELL Quest software.

3. Results and discussion

3.1. Modeling, synthesis and characterization of the nanocomposite

The state of self-assembled Gd₂O₃ molecules inside the mesopores of silica is vital to the contrast enhancement and toxicity of the nanocomposite. In order to investigate the bonding characteristic between the Gd₂O₃ molecules and silica matrix, we calculated the adsorption energy of Gd₂O₃ molecules on silica matrix as well as the Mulliken charge distribution and electron population using the density functional theory (DFT) (Fig. 1 and SI 1.1). The adsorption energy E_a is -5.02966 eV, indicating that Gd₂O₃ molecules could be absorbed by silica matrix. The Mulliken charge and population of electron shells of atoms before and after adsorption of Gd₂O₃ molecule were calculated (Table 1). There exists a strong covalent bonding between Si of silica matrix and O of Gd₂O₃ molecule as revealed by the considerable variation of both Mulliken charge and population of electron shells. The difference between the formal ionic charge and the Mulliken charge indicates the levels of the ionic bond. A value of zero indicates a perfect ionic bond. Since the calculated transferred charge indicates some ionic interaction between the elements, it could be inferred that the bonding behavior of atoms between Gd₂O₃ molecule and silica matrix is a combination of ionic and covalent natures. Judging from the Mulliken charge distribution and electron population before and after adsorption, we conclude that a sort of strong chemical adsorption occurs between Gd₂O₃ molecule and silica matrix with a combination of ionic and covalent bonds. There are hardly any Gd₂O₃ molecules or Gd ions dissociated from the silica matrix. Therefore, estimated by the calculation above, Gd₂O₃ molecules assembled inside mesopores of silica are theoretically toxicity-free and potentially accessible by water molecules through the mesopores to the Gd atoms.

Molecular dynamic simulation and experimental measurements further revealed the microstructure and performance of the Gd₂O₃-assembled MCM-41 silica nanocomposite (SI 1). We captured the overall morphology of the synthesized nanocomposite with a 5.7 at.% Gd doping (Fig. 2A) and compare the simulated supercell of Gd₂O₃@MCM-41 with the high-resolution transmission electron microscope (HRTEM) images (insets of Fig. 2A). The nanoparticles are averaged about 86 nm in size with good dispersion and sphericity (Fig. 2A,B). The simulated and observed microstructures of the nanocomposite take on a hexagonal array of mesopores. The Gd₂O₃ clusters (each cluster consists of five Gd₂O₃ molecules) were simulated located on the inner surface of the mesopores in its equilibrium state, as observed by the dark spots in the magnified HRTEM view (3 nm scale bar). The dispersive dark-spots (~ 1 nm) adjacent to the hexagonal pores have been identified further the Gd-containing clusters by the energy dispersive X-ray spectroscopy (EDS) (Fig. 2C). The Gd₂O₃ clusters (~ 1 nm) have been indeed incorporated into the mesopores (~ 2.9 nm) of silica MCM-41 (insets of Fig. 2A). The small-angle X-ray diffraction (XRD) pattern of the supercell was simulated and compared with its experimental counterparts (Fig. 2D). Two XRD patterns are in good agreement

with each other, indicating that both the simulated model and synthesized nanoparticles have the characteristic of a long-range ordered hexagonal MCM-41 array. The assembly of Gd₂O₃ nanocluster has not resulted in any disruption of the hexagonal array of MCM-41 mesoporous silica.

Contrast enhancement of an MRI medium depends on both the accessibility of water molecules to Gd ions and the proton relaxivity r_1 of water molecules adsorbed within silica matrix. The proton relaxivity is adjustable by the presence of neighboring Gd ions when a magnetic field is applied [36]. We next compared water adsorption of simulated models with experimentally measured samples assembled with different additions of the Gd₂O₃ molecule (Fig. 3a). The water adsorption of MCM-41 silica matrix decreases with Gd-doping. By comparing the relaxivity r_1 and T_1 -weighted phantom MR image between the Gd₂O₃@MCM-41 silica nanocomposite and Gd-DTPA (the commercially available contrast agent Magnevist®), we show that our nanocomposite has a better contrast enhancement (Fig. 3b and c).

3.2. In vitro and in vivo assessment of biocompatibility and pharmacodynamics of Gd₂O₃@MCM-41 silica nanocomposite

3.2.1. In vitro study

Cell viability was determined by incubating the fibrosarcoma cell line L-929 of mouse and the murine macrophage line RAW264.7 with different concentrations of Gd₂O₃@MCM-41 at 48 h (Fig. 4a) and 72 h (SI Fig. 2). There were no significant differences between the nanocomposite and the control (culture media and solvent) for both cell lines, suggesting that the nanocomposite has no toxicity to the cell lines. Activated RAW264.7 cells phagocytose foreign nanoparticles and secrete chemical mediators [37]. These cells are instrumental in regulating the immune system during the process of phagocytosis. Cell cycle and apoptosis were assessed by flow cytometry (BD FACS Calibur) at 48 h, in comparison with Gd-DTPA treated cells (Fig. 4b, SI Fig. 4a). Cellular uptake of the nanocomposite (5 μ M) by RAW264.7 cells was observed using confocal microscope (Carl Zeiss AG) (SI Fig. 3).

3.2.2. In vivo study

The data on the immunotoxicity and acute toxicity of the nanocomposite is presented in Fig. 4. No obvious change was observed in the Kupffer cells, indicating that no immunological reaction occurred after the injection of the nanocomposites (32 μ mol/kg). We thus conclude that the nanocomposite do not present potential immunotoxicity, and nor do lead to the production of free gadolinium ions.

Acute toxicity assay shows that the median lethal dose (LD₅₀) is 72.7 mg/kg with 95% confidence limits from 68.9 to 76.7 mg/kg (Fig. 4f). We harvested organs of the dead mice and HE-stained tissue slices after injection in mice (99.43 mg/kg) (Fig. 4f). Edema was significantly showed in kidney, liver, lung and spleen; degeneration was found in kidney, liver, heart, and spleen. Pulmonary embolism and coronary thrombotic occlusion appear to be the cause of death. Mice that survived (group 6 in SI Table 1) and mice of the control group did not show any abnormalities.

The density of blood is 1.057 g/mL [38], and the half-life was 97.26 min, as assessed by straight-line regression analysis (Fig. 5a). Compared with the 20 min half-life of Gd-DTPA [39], the nanocomposite can be retained longer in the blood. More than 90% of gadolinium was cleared from the blood within 400 min, suggesting that the nanocomposite is a superior contrast medium in the bloodstream with low blood toxicity.

Quantitative analysis on the biodistribution of the nanocomposite in tumor tissues and organs at cellular and subcellular

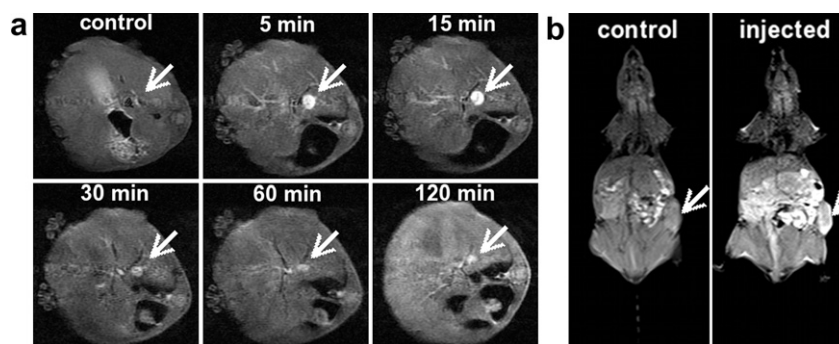


Fig. 6. (a) MR images of dynamic enhancement of mouse vasculature at 0, 5, 15, 30, 60 and 120 min after intravenous administration of $\text{Gd}_2\text{O}_3\text{@MCM-41}$ nanoparticles ($16 \mu\text{mol/kg}$); (b) T_1 -weighted MR images demonstrate significant signal enhancement in NPC CNE-2 xenografted tumor (white arrow), control (Left) and post-contrast (Right) ($16 \mu\text{mol/kg}$).

levels was conducted using ICP-MS (Calibration curve for Gd is shown in SI Fig. 5). The nanocomposite is gradually accumulated in liver, spleen and tumor, and strongly accumulated in lung already 1 h after injection. There was minimal gadolinium detected in capillary pericytes, and few nanocomposites were found in the brain, heart and kidney. Nanoparticles were more prone to enter and accumulate in tumor tissues than normal tissues via capillaries and repeated blood with modified nanoparticles in combination with conjugated ligand and antibody [40,41]. The blood–brain barrier (BBB) is impermeable to particles with diameters greater than 20 nm [42]. It is therefore difficult for the nanocomposite to penetrate into the brain. Lastly, no abnormal changes were observed in histological sections of the lung, liver, kidney, spleen and heart, indicating that tissue morphology and cellular integrity are not affected by the nanocomposite (SI Fig. 6).

At the subcellular level, sections of liver, spleen, lung and the nasopharyngeal carcinoma (NPC) tissue were observed by TEM (100-CX, JEOL) (Fig. 5c). The nanoparticles are mainly compartmentalized in lysosomes of macrophage in the liver or spleen, in an endocytic vesicle in lung and the NPC tissue (24 h post-tail vein injection), very few in brain and kidney (SI Fig. 7).

The Gd concentration in both feces and urine of mice were measured by ICP-MS (Fig. 5d) every week after nanocomposite injection. About 25% of nanocomposites excreted via the hepatobiliary pathway within the first week, 50% nanocomposite were excreted about after 6 weeks, followed by a gradual decrease in further excretion. Although hepatobiliary excretion is a slow process, it can effectively clear the nanocomposite without any sign of organ toxicity.

The nanocomposite owns a better *in vitro* MRI contrast enhancement than Gd-DTPA (Fig. 3b and c). MR images *in vivo* (Fig. 6) show that the concentration of the nanocomposite is optimal for MRI detection of the tumor at about 30 min post-injection via passively targeted accumulation, which is consistent with the distribution results. Collectively, the data above justify the feasibility of the $\text{Gd}_2\text{O}_3\text{@MCM-41}$ nanocomposite as a safe and effective MRI contrast agent.

4. Conclusions

Our systematical study of Gd_2O_3 -assembled mesoporous silica MCM-41 nanocomposite has identified both *in vitro* and *in vivo* the nanocomposite as a safe MRI contrast medium with better efficacy than its commercially available counterpart Gd-DTPA. Our pre-clinical research of this nanocomposite paves the way for its further clinical investigation, such as long-term toxicity and metabolism studies. The unique nanostructure of the nanocomposite qualifies it to be developed into a potential targeted nanoprobe for early tumor diagnosis.

Acknowledgments

This work was supported by the funds from the NSFC of China (81071207, 10875178) and Specialized Research Fund for the Doctoral Program of Higher Education (20110171110023), the Fundamental Research Funds for the Central Universities (10ykjcll), and the Open Funds of State Key Laboratory of Oncology in South China (HN2011-02).

Appendix A. Supplementary data

Supplementary data associated with this article can be found, in the online version, at doi:10.1016/j.biomaterials.2012.05.065.

References

- [1] Gao J, Gu H, Xu B. Multifunctional magnetic nanoparticles: design, synthesis, and biomedical applications. *Acc Chem Res* 2009;42:1097–107.
- [2] Louie A. Multimodality imaging probes: design and challenges. *Chem Rev* 2010;110:3146–95.
- [3] Weissleder R, Pittet MJ. Imaging in the era of molecular oncology. *Nature* 2008;452:580–9.
- [4] Rosenholm JM, Peuhu E, Eriksson JE, Sahlgren C, Lindén M. Targeted intracellular delivery of hydrophobic agents using mesoporous hybrid silica nanoparticles as carrier systems. *Nano Lett* 2009;9:3308–11.
- [5] Vallet-Regí M, Balas F, Arcos D. Mesoporous materials for drug delivery. *Angew Chem Int Ed* 2007;46:7548–58.
- [6] Barbe C, Bartlett J, Kong L, Finnie K, Lin HQ, Larkin M, et al. Silica particles: a novel drug-delivery system. *Adv Mater* 2004;16:1959–66.
- [7] Kneuer C, Sameti M, Haltner EG, Schiestel T, Schirra H, Schmidt H, et al. Silica nanoparticles modified with aminosilanes as carriers for plasmid DNA. *Int J Pharm* 2000;196:257–61.
- [8] Roy I, Ohulchanskyy TY, Bharali DJ, Pudavar HE, Mistretta RA, Kaur N, et al. Optical tracking of organically modified silica nanoparticles as DNA carriers: a nonviral, nanomedicine approach for gene delivery. *P Natl Acad Sci USA* 2005;102:279–84.
- [9] Yu H, Zhai Q-Z. Mesoporous SBA-15 molecular sieve as a carrier for controlled release of nimodipine. *Microporous Mesoporous Mater* 2009;123:298–305.
- [10] Sumer B, Gao J. Theranostic nanomedicine for cancer. *Nanomedicine* 2008;3:137–40.
- [11] Selvi BR, Jagadeesan D, Suma BS, Nagashankar G, Arif M, Balasubramanyam K, et al. Intrinsically fluorescent carbon nanospheres as a nuclear targeting vector: delivery of membrane-impermeable molecule to modulate gene expression in vivo. *Nano Lett* 2008;8:3182–8.
- [12] Shan L. Gadolinium-incorporated mesoporous silica nanoparticles. Gadolinium-incorporated mesoporous silica nanoparticles. *Mol Imaging Contrast Agent Database (MICAD)* [database online].
- [13] van Schooneveld MM, Vucic E, Koole R, Zhou Y, Stocks J, Cormode DP, et al. Improved biocompatibility and pharmacokinetics of silica nanoparticles by means of a lipid coating: a multimodality investigation. *Nano Lett* 2008;8:2517–25.
- [14] Zhu Z-J, Carboni R, Quercio MJ, Yan B, Miranda OR, Anderton DL, et al. Surface properties dictate uptake, distribution, excretion, and toxicity of nanoparticles in fish. *Small* 2010;6:2261–5.
- [15] Kumar R, Roy I, Ohulchanskyy TY, Goswami LN, Bono AC, Bergey EJ, et al. Covalently dye-linked, surface-controlled, and bioconjugated organically modified silica nanoparticles as targeted probes for optical imaging. *ACS Nano* 2008;2:449–56.

- [16] Oberdörster G, Oberdörster E, Oberdörster J. Concepts of nanoparticle dose metric and response metric. *Environ Health Perspect* 2007;115:A290.
- [17] Fischer HC, Chan WCW. Nanotoxicity: the growing need for in vivo study. *Curr Opin Biotechnol* 2007;18:565–71.
- [18] Dobrovolskaia MA, McNeil SE. Immunological properties of engineered nanomaterials. *Nat Nanotechnol* 2007;2:469–78.
- [19] Fadeel B, Garcia-Bennett AE. Better safe than sorry: understanding the toxicological properties of inorganic nanoparticles manufactured for biomedical applications. *Adv Drug Deliv Rev* 2010;62:362–74.
- [20] Mohammadi-Nejad A-R, Hossein-Zadeh G-A, Soltanian-Zadeh H. Quantitative evaluation of optimal imaging parameters for single-cell detection in MRI using simulation. *Magn Reson Imaging* 2010;28:408–17.
- [21] Petri-Fink A, Hofmann H. Superparamagnetic iron oxide nanoparticles (SPIONs): from synthesis to in vivo studies—a summary of the synthesis, characterization, in vitro, and in vivo investigations of SPIONs with particular focus on surface and colloidal properties. *IEEE Trans Nanobiosci* 2007;6:289–97.
- [22] Cho M, Cho W-S, Choi M, Kim SJ, Han BS, Kim SH, et al. The impact of size on tissue distribution and elimination by single intravenous injection of silica nanoparticles. *Toxicol Lett* 2009;189:177–83.
- [23] He Q, Zhang Z, Gao Y, Shi J, Li Y. Intracellular localization and cytotoxicity of spherical mesoporous silica nano- and microparticles. *Small* 2009;5:2722–9.
- [24] Carrero-Sanchez JC, Elías AL, Mancilla R, Arrellín G, Terrones H, Laclette JP, et al. Biocompatibility and toxicological studies of carbon nanotubes doped with nitrogen. *Nano Lett* 2006;6:1609–16.
- [25] Burns AA, Vider J, Ow H, Herz E, Penate-Medina O, Baumgart M, et al. Fluorescent silica nanoparticles with efficient urinary excretion for nanomedicine. *Nano Lett* 2009;9:442–8.
- [26] Taylor KML, Kim JS, Rieter WJ, An H, Lin W, Lin W. Mesoporous silica nanospheres as highly efficient MRI contrast agents. *J Am Chem Soc* 2008;130:2154–5.
- [27] Shao Y-Z, Liu L-Z, Song S-Q, Cao R-H, Liu H, Cui C-Y, et al. A novel one-step synthesis of Gd³⁺-incorporated mesoporous SiO₂ nanoparticles for use as an efficient MRI contrast agent. *Contrast Media Mol Imaging* 2011;6:110–8.
- [28] Bhakta G, Sharma RK, Gupta N, Cool S, Nurcombe V, Maitra A. Multifunctional silica nanoparticles with potentials of imaging and gene delivery. *Nanomedicine* 2011;7:472–9.
- [29] Selvan ST, Tan TTY, Yi DK, Jana NR. Functional and multifunctional nanoparticles for bioimaging and biosensing. *Langmuir* 2010;26:11631–41.
- [30] Li S, Liu H, Li L, Luo N-Q, Cao R-H, Chen D-H, et al. Mesoporous silica nanoparticles encapsulating Gd₂O₃ as a highly efficient magnetic resonance imaging contrast agent. *Appl Phys Lett* 2011;98:093704.
- [31] Gordon S, Lawson L, Rabinowitz S, Crocker PR, Morris L, Perry VH. Antigen markers of macrophage differentiation in murine tissues. *Curr Top Microbiol* 1992;181:1–37.
- [32] Wink DA, Hines HB, Cheng RYS, Switzer CH, Flores-Santana W, Vitek MP, et al. Nitric oxide and redox mechanisms in the immune response. *J Leukoc Biol* 2011;89:873–91.
- [33] Sancho D, Gómez M, Sánchez-Madrid F. CD69 is an immunoregulatory molecule induced following activation. *Trends Immunol* 2005;26:136–40.
- [34] Lenschow DJ, Walunas TL, Bluestone JA. CD28/B7 system of T cell costimulation. *Annu Rev Immunol* 1996;14:233–58.
- [35] Hsu SM, Raine L, Fanger H. The use of avidin antibody and avidin-biotin-peroxidase complex in immunoperoxidase techniques. *Am J Clin Pathol* 1981;75:816–21.
- [36] Cheon J, Lee J-hyun. Synergistically integrated nanoparticles as multimodal probes for nanobiotechnology. *Acc Chem Res* 2008;41:1630–40.
- [37] Pulskamp K, Diabaté S, Krug HF. Carbon nanotubes show no sign of acute toxicity but induce intracellular reactive oxygen species in dependence on contaminants. *Toxicol Lett* 2007;168:58–74.
- [38] Marque V, Kieffer P, Gayraud B, Lartaud-Ijdouadiene I, Ramirez F, Atkinson J. Aortic wall mechanics and composition in a transgenic mouse model of marfan syndrome. *Arterioscler Thromb Vasc Biol* 2001;21:1184–9.
- [39] Weinmann H, Brasch R, Press W, Wesbey G. Characteristics of gadolinium-DTPA complex: a potential NMR contrast agent. *Am J Roentgenol* 1984;142:619–24.
- [40] Roy I, Ohulchanskyy TY, Pudavar HE, Bergey EJ, Oseroff AR, Morgan J, et al. Ceramic-based nanoparticles entrapping water-insoluble photosensitizing anticancer drugs: a novel drug-carrier system for photodynamic therapy. *J Am Chem Soc* 2003;125:7860–5.
- [41] De Jong WH, Hagens WL, Krystek P, Burger MC, Sips AJAM, Geertsma RE. Particle size-dependent organ distribution of gold nanoparticles after intravenous administration. *Biomaterials* 2008;29:1912–9.
- [42] Sonavane G, Tomoda K, Makino K. Biodistribution of colloidal gold nanoparticles after intravenous administration: effect of particle size. *Colloids Surface B* 2008;66:274–80.